Construction and Building Materials 445 (2024) 137806

Contents lists available at ScienceDirect

Construction and Building Materials

journal homepage: www.elsevier.com/locate/conbuildmat

Behaviour of Textile Reinforced Concrete panels under high-velocity impact loading

Mohamed Esaker *, Georgia E. Thermou, Luis Neves

Department of Civil Engineering, University of Nottingham, University Park, Nottingham NG7 2RD, UK

ARTICLE INFO

Keywords:
Textile Reinforced Concrete (TRC)
High velocity
Impact load
Carbon
Glass
Fibres

ABSTRACT

This study aims to experimentally investigate the impact resistance of Textile Reinforced Concrete (TRC) panels under high-velocity impact loading. 54 control and TRC panels were fabricated using a standard (29 MPa) and a high (101 MPa) compressive strength concrete, as well as Ultra-High-Performance Fibre Reinforced Cementitious Composites (UHPFRCCs) (132 MPa). 36 out of 54 TRC panels were reinforced with carbon and glass textiles. The mechanical properties of all types of composite systems were investigated under four-point bending test. All specimens were subjected to a high-velocity impact load from a hemispherical steel projectile travelling with an initial impact velocity ranging from ~60 m.s^{-1} to ~160 m.s^{-1}. A high-speed camera was used to track the projectile and record the impact process. The level of impact damage to the TRC panels was quantified by the mass loss, penetration depth and scabbing diameter. The results demonstrated that the standard compressive strength concrete had a flexural toughness 17 % higher than that of the higher compressive strength. The most efficient system in reducing crack propagation and local damage against high-velocity (160 m.s^{-1}) projectile impact load was the UHPFRCCs reinforced with carbon textiles, resulting in maximum penetration depth 25 % lower compared to unreinforced UHPFRCCs panels.

1. Introduction

In recent decades, there has been a growing interest in the performance of buildings and infrastructure when subjected to severe loading conditions [1]. Due to the fact that concrete is a material that is frequently employed in the construction industry, its performance under severe loading conditions, such as impact loading, has been the subject of multiple investigations. Concrete structures may experience localised impact from small, high-velocity projectiles resulting from blast-induced fragments or flying objects produced by forces of nature such as tornadoes or volcanoes. These missiles exhibit significant variations in their shapes and sizes, as well as in their velocities, stiffness, and orientation upon impact. Consequently, they cause a diverse range of damage to the structure. When concrete structures are subjected to high-velocity impact loading, small fragments can be generated from the back face spalling due to the low tensile strength of concrete. As a result of the impact event, these fragments have the potential to move at a high velocity, which poses a risk to the safety of the occupants of the structure as well as those who are in the surrounding area. Therefore, improving the strength of concrete elements can reduce the hazard related to debris and thereby reduce the local damage.

Conventional concrete can behave in various different ways when subjected to severe loading according to the brittle characteristics, tensile strength, and the capacity to absorb energy. Thus, for the limitations of conventional concrete to be overcome, numerous different forms of fibre-reinforced concrete (FRC) have been developed [2–8]. From the various types available, discontinuous fibres are generally preferred for concrete as they can be easily incorporated into the concrete mixture and render the concrete more resistant to impact as a result of their ability to bridge cracks. A specific type of such concrete, Ultra-High-Performance Fibre-Reinforced Concrete (UHPFRC) has exhibited enhanced dynamic behaviour after having been exposed to impacts from high-velocity projectiles with regard to the penetration depth, cratering damage, and crack propagation because the addition of fibres can generally prevent such cracks from forming, thus limiting any potential damage [9–13]. Yoo and Banthia [14] conducted an investigation of the effects of the size of the specimen, orientation of fibres, fibre properties, and loading rate on UHPFRC's resistance to impacts and blasts, presenting a summary of the general manner in which the material behaved. According to the findings, if fibre volumetric content

* Corresponding author.
E-mail address: mohamed.esaker@nottingham.ac.uk (M. Esaker).

https://doi.org/10.1016/j.conbuildmat.2024.137806
Received 7 April 2024; Received in revised form 29 July 2024; Accepted 5 August 2024
Available online 16 August 2024

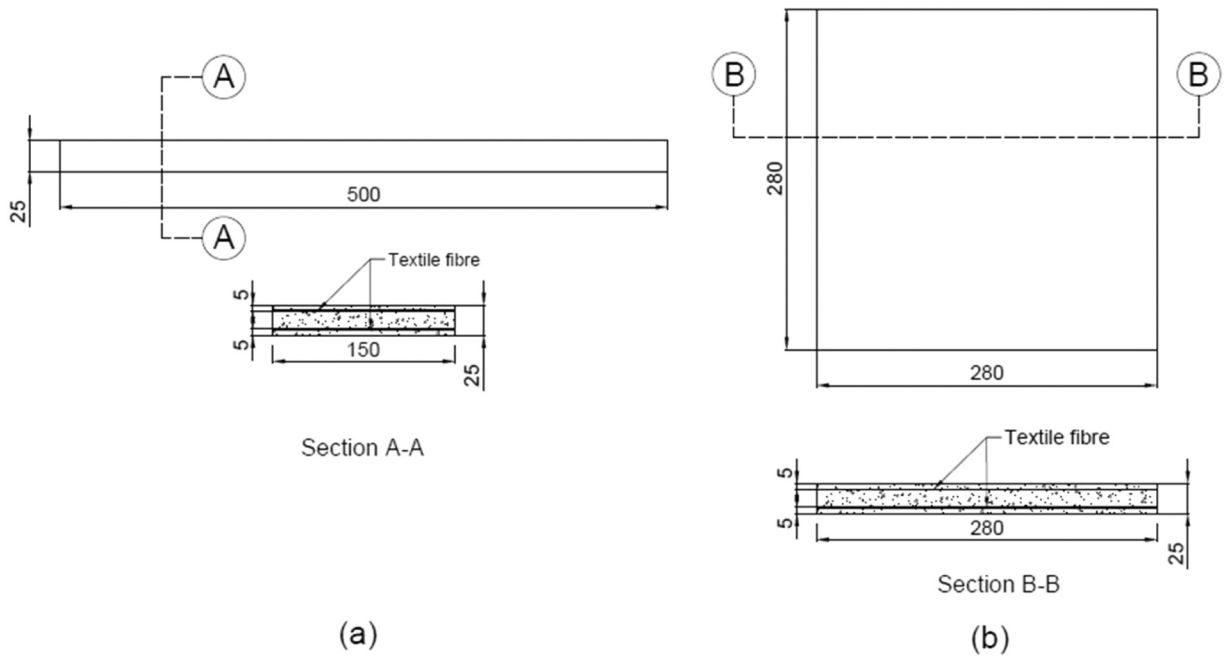

Fig. 1. Geometry and cross section of the TRC: (a) Beams, (b) Panels. Note all dimensions are in mm.

increased above 2 %, the ability of UHPFRC to resist impacts was not significantly enhanced [15–18]. The main conclusions regarding impact penetration reported in the experimental research conducted by O'Neil et al. [19] received support from the studies undertaken by Anderson et al. [20] and Dancygier and Yankelevsky [21], who found that although observable damage was reduced by incorporating fibres, the strength of the concrete was not significantly reduced in terms of the depth of penetration.

The effect of steel wire mesh on the projectile impact resistance of concrete structures was investigated by [22,23]. The researchers incorporated 44 layers of steel mesh into the reactive powder concrete targets, providing a protective layer of 6 mm. The targets were impacted by steel projectiles with ogive-shaped noses, striking at impact velocities between 550 m/s and 800 m/s. The results demonstrated that the steel wire mesh reinforcement significantly improved the impact resistance in terms of both penetration depth and crater diameter. In the study conducted by Maalej et al. [24], the behaviour of engineered cementitious composites (EEC) under projectile impact and dynamic tensile stress was investigated in comparison with standard concrete. The results indicated that the resistance to impact of ECC was enhanced with a reduction in the damage zone, scabbing, and spalling in addition to an increased capacity to absorb energy. Nevertheless, a significant decrease in the depth of penetration was not observed.

Other studies in the literature [16,25–29] have reported that if the toughness and strength of the cementitious matrix is enhanced, this can efficiently increase the capacity of the concrete to resist impact. Kim et al. [29] conducted an investigation in which the resistance to impact of two distinct types of materials, namely strength-oriented Ultra-High Performance Fibre Reinforced Concrete (UHPFRC) and ductility-oriented alkali-activated slag-based High-Ductility Fibre Reinforced Concrete (HDFRC), when exposed to impact load from a high-velocity projectile impact loading. They found that the toughness of UHPFRC, whose compressive strength and tensile capacity are 155 MPa and 1.04 %, respectively, was almost similar to that exhibited by the HDFRC mixture whose compressive strength and tensile strain capacity were 32.9 MPa and 7.9 %. In addition to this, it was found that the HDFRC had an impact resistance that was nearly identical to that of the UHPFRC in terms of mode of failure, scabbing diameter, and depth of penetration.

Ramesh et al. [30] performed a study on the effect of low velocity impact loading on 3D-printed TRC using a drop weight. The study investigated two types of textile reinforcement, including AR-glass and carbon, in high-strength concrete panels that were produced using 3D printing. The findings demonstrated that the use of textile reinforcement, particularly carbon, substantially enhanced the impact resistance, energy absorption capacity, and damage distribution in comparison to specimens without reinforcement. Moreover, the findings indicated that the utilisation of carbon textile reinforcement led to a 75 % enhancement in impact resistance, as compared to AR-glass reinforcement. This improvement can be attributed to the higher stiffness and strain-hardening properties of carbon textile reinforcement.

The use of FRC in high-velocity impact loading has several disadvantages. Murali et al. [31] found that while FRC can improve impact resistance, it still experiences a reduction in strength under impact loads. Kim et al. [3] further noted that the penetration depth of FRC increases with higher steel volume fractions, indicating a potential limitation in its impact resistance. Banthia et al. [32] and Ong et al. [33] both highlighted the potential for improved impact resistance with the use of steel fibres, but also noted that the effectiveness of these fibres can be influenced by factors such as temperature and the type of fibres used.

As demonstrated above, the use of FRC and steel wire mesh significantly improves the impact resistance under high-velocity impact loading. However, both types of reinforcement have some drawbacks such as: the random distribution of fibres that limits its performance, as fibres cannot be guaranteed to be distributed within the desired location and direction. Also, the use of steel wire mesh as reinforcement in concrete panels raises questions concerning its suitability and durability. The small diameter of the wires (0.5 mm to 2 mm), which increases the inherent sensitivity of steel to corrosion, can cause gradual deterioration of the reinforcement over time, affecting the overall structural integrity of the panels and therefore their impact resistance. Thus, these considerations indicate it is necessary to investigate new types of protective materials with high durability, tensile capacity and ductility [34,35] to absorb the impact energy and therefore resist high-velocity impact loads such as TRC. The present study aims to assess how enhancing the strength and ductility of cementitious materials affects their performance under high-velocity impact conditions. This will be achieved by comparing the performance of standard and high strength concrete as

Table 1
Type and number of specimens used in impact test, and four-point bending test.

Specimen ID	Mortar type	Fibre type	Textile type	Dimensions (mm)	No. of specimens	Test name
P-M1-*l*	M1	NA	NA	280 ×280 x 25	2	High-velocity impact load
P-M1-*m*	M1	NA	NA		2	
P-M1-*h*	M1	NA	NA		2	
P-M1-C-*l*	M1	NA	Carbon		2	
P-M1-C-*m*	M1	NA	Carbon		2	
P-M1-C-*h*	M1	NA	Carbon		2	
P-M1-G-*l*	M1	NA	Glass		2	
P-M1-G-*m*	M1	NA	Glass		2	
P-M1-G-*h*	M1	NA	Glass		2	
P-M2-*l*	M2	NA	NA		2	
P-M2-*m*	M2	NA	NA		2	
P-M2-*h*	M2	NA	NA		2	
P-M2-C-*l*	M2	NA	Carbon		2	
P-M2-C-*m*	M2	NA	Carbon		2	
P-M2-C-*h*	M2	NA	Carbon		2	
P-M2-G-*l*	M2	NA	Glass		2	
P-M2-G-*m*	M2	NA	Glass		2	
P-M2-G-*h*	M2	NA	Glass		2	
P-UHP-l	UHPFRCC	Steel	NA		2	
P-UHP-m	UHPFRCC	Steel	NA		2	
P-UHP-h	UHPFRCC	Steel	NA		2	
P-UHP-C-l	UHPFRCC	Steel	Carbon		2	
P-UHP-C-m	UHPFRCC	Steel	Carbon		2	
P-UHP-C-h	UHPFRCC	Steel	Carbon		2	
P-UHP-G-l	UHPFRCC	Steel	Glass		2	
P-UHP-G-m	UHPFRCC	Steel	Glass		2	
P-UHP-G-h	UHPFRCC	Steel	Glass		2	
B-M1	M1	NA	NA	500 ×150 x 25	3	Four-point bending test
B-M1-C	M1	NA	Carbon		3	
B-M1-G	M1	NA	Glass		3	
B-M2	M2	NA	NA		3	
B-M2-C	M2	NA	Carbon		3	
B-M2-G	M2	NA	Glass		3	
B-UHP	UHPFRCC	Steel	NA		3	
B- UHP-C	UHPFRCC	Steel	Carbon		3	
B- UHP-G	UHPFRCC	Steel	Glass		3	

well as UHPFRCCs reinforced using glass and carbon textiles. Fifty-four control and TRC panels were subjected to high-velocity impact loads from a non-deformable hemispherical steel projectile, which was fired from a compressed air gun, travelling with initial impact velocities ranging from ~60 m.s^{-1} to ~160 m.s^{-1}. The currently available empirical formulas for predicting penetration depth were examined and found to be insufficient when applied to samples that include fibres or textile materials.

2. Experimental programme

2.1. Specimen details

This study aimed to investigate the impact performance of TRC by evaluating the effects of two variables: concrete strength and type of textile. The variables were carefully selected according to the findings drawn from a prior review paper published by the authors [36] on the impact resistance of concrete and fibre-reinforced concrete. Based on this analysis, the authors have found that the impact performance of concrete panels is primarily influenced by two key factors: the strength of the concrete and the type and configuration of reinforcement. The thickness of the specimens was chosen based on the typical application of TRC panels, which are frequently designed as thin and shell-like structures.

In this experimental study, two sets of TRC specimens were fabricated: (i) beams with dimensions of "500 mm (length) x 150 (width) mm x 25 (height) mm" and 280 mm square panels with 25 mm in thickness (Fig. 1). The beams were used to quantify the mechanical properties of TRC whereas the panels were used to evaluate their impact performance. Two layers of textiles "glass or carbon" were embedded in standard "M1" and high "M2" compressive strength ready-mixed mortars. The layout of the embedded reinforcement is presented in Fig. 1. Additionally, a hybrid system was studied where UHPFRCCs were combined with the glass or carbon textiles.

The identification codes follow the notation XYZW, where X stands for the type of specimen (B for beams, P for panels), Y stands for the type of mixture (M1 for standard strength "29 MPa", M2 for high strength "101 MPa", UHP for UHPFRCCs "132 MPa", Z stands for the type of fibre textile reinforcement (C for carbon, G for glass), W stands for the velocity (*l* for low velocity "60–90 m.s^{-1}", *m* for medium velocity "80–120 m.s^{-1}", *h* for high velocity "90–160 m.s^{-1}". For the high-velocity impact loading test, six panels were constructed for each specimen type (in total 54 panels) whereas for the four-point bending test, three beams were constructed for each specimen type (in total 27 beams). The details of the specimen are presented in Table 1.

2.2. Materials properties

2.2.1. Mortars

A standard and a high compressive strength commercial cement-based mortars (M1 and M2, respectively) were used as the matrix of the TRC. M1 is a two-component, standard-strength cement- and high ductility pozzolanic-reactive based mortar and M2 is a high strength ready-mixed free-flowing mortar that include 0.25 % of Mapecure to promote early and efficient hydration of the mortar. M2 mortar also includes Shrinkage-Reducing Admixture (SRA) to reduce the plastic and hydraulic shrinkage that could be caused due to the dense microstructure and low water-to-cement ratio of the mix. The ready mixes were prepared with water to cement ratios of 0.27 and 0.12 for M1 and M2, respectively. In addition, UHPFRCC was used where 1.625 kg of copper-coated chopped steel fibres were added to each 25 kg of M2, therefore, the volume fraction of steel fibres in the mix was 1.4 %. The mechanical

Table 2
Mechanical and physical properties of steel fibres.

Shape	Density (g/cm^3)	Length (mm)	Diameter (mm)	Tensile strength (MPa)	Modules of elasticity (GPa)
Straight	7.85	13	0.21	2750	200

Table 3
Mechanical and physical properties of ready-mix mortars.

Mortar type	Bulk density (Kg/m^3)	Compressive strength (MPa) (STD*)	Modules of elasticity (GPa)
M1	1200	29.2 (1.02)	10
M2	1400	100.6 (2.61)	28
UHPFRCC	1700	131.9 (6.78)	37

*STD: Standard Deviation

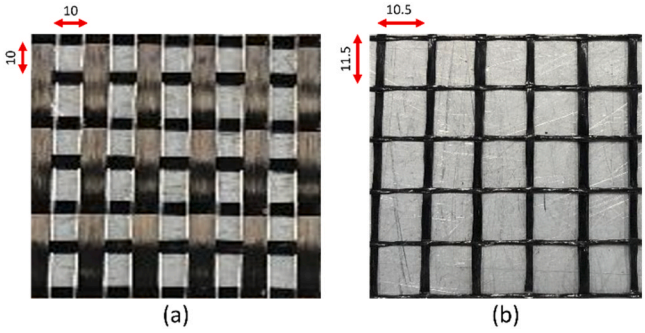

Fig. 2. Types of textiles: (a) Carbon, and (b) Glass textile (dimensions in mm).

and physical properties of the steel fibres are presented in Table 2.

The average compressive strengths of the matrices were obtained from three 50 mm cubes for each mortar in accordance with BS EN 12390–3:2009 [37] at 28 days. The main mechanical properties of the mortars used are listed in Table 3.

2.2.2. Textiles

In order to internally reinforce the concrete, two types of textile fibre were employed in this study: a mesh constructed from primed, alkali-resistant (AR) glass fibres containing 17 % zirconia in a weaved design, and a square mesh constructed from carbon fibres with increased strength (Fig. 2b). Tensile tests were performed in order to determine the textiles' mechanical characteristics. For the separate textiles, five strips comprised six yarns with dimensions of 400 mm×50 mm were cut then adhered to 50 mm×60 mm, with glue applied to both ends of the strips, as illustrated in Fig. 3a and b. An INSTRON universal tensile testing device was used to perform the testing with a loading rate of 2 mm/min [38]. Deformations were monitored using a video gauge, whereas the load was measured with a load cell (Fig. 3c). The textiles' physical and mechanical characteristics are detailed in Table 4.

2.3. Preparation of the specimens

The process of preparing the fresh mixtures of M1 and M2 involved blending the dry particles (powder) for 2 mins with mixer capacity of 0.01 m^3, followed by the gradual addition of water to the mix. Continuous blending of the mix was then performed until the mixture had sufficient flowability to enable the fibres to be distributed. To ensure that the steel fibres were uniformly distributed throughout the cementitious mixture for the specimens of UHPFRCC, the process of adding the steel fibres to the fresh mix was carefully performed manually, followed by continuous blending of the mix for 2 min. The resulting mix was then poured into moulds to form the beams and panels. The formwork moulds designed for the beam specimens had dimensions of 500 mm × 150 mm

Table 4
Mechanical and physical properties of carbon and glass textiles.

Type of textile fibres	Weight (g/m^2)	Mesh size (mm)	Thickness (mm)	Tensile strength (KN/m)	Modules of elasticity (GPa)
Carbon	170	10 ×10	0.048	250	252
Glass	120	10.5 ×11.5	0.024	30	70

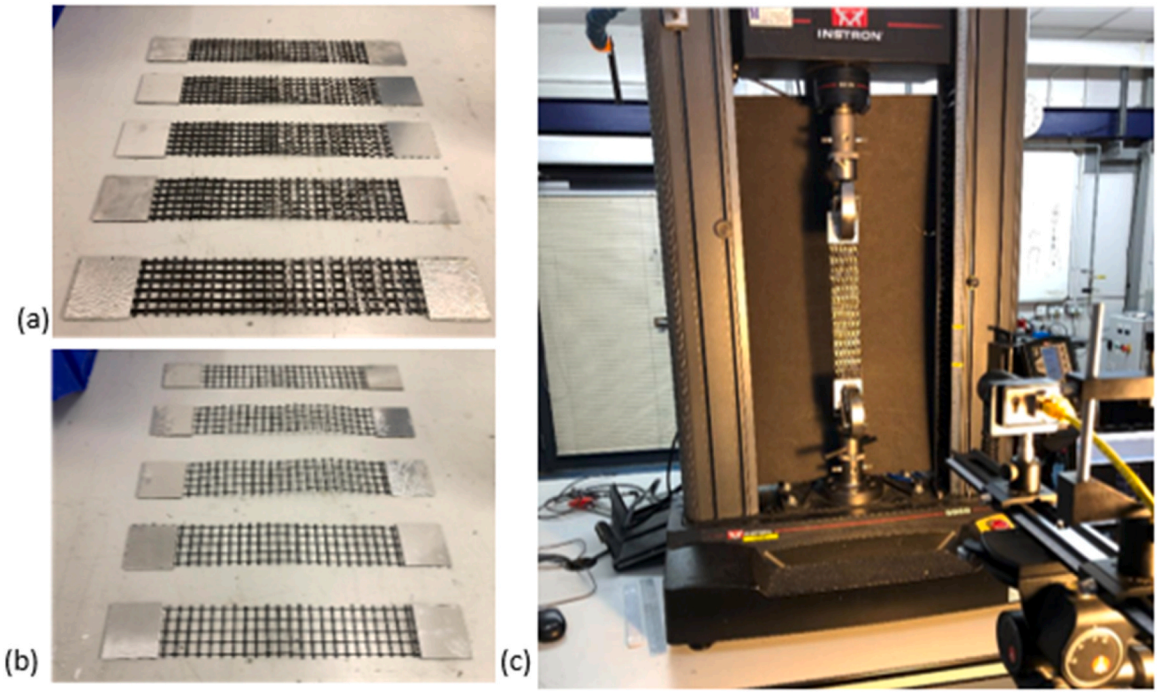

Fig. 3. (a) Carbon textile strips, (b) Glass textile strips, (c) Tensile test setup.

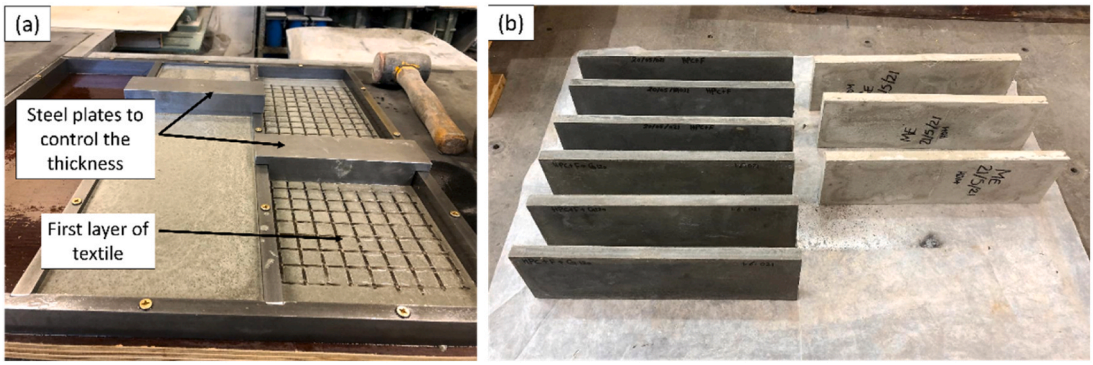

Fig. 4. Construction of beams (a) Casting of the beams, (b) Demoulding the beams after casting.

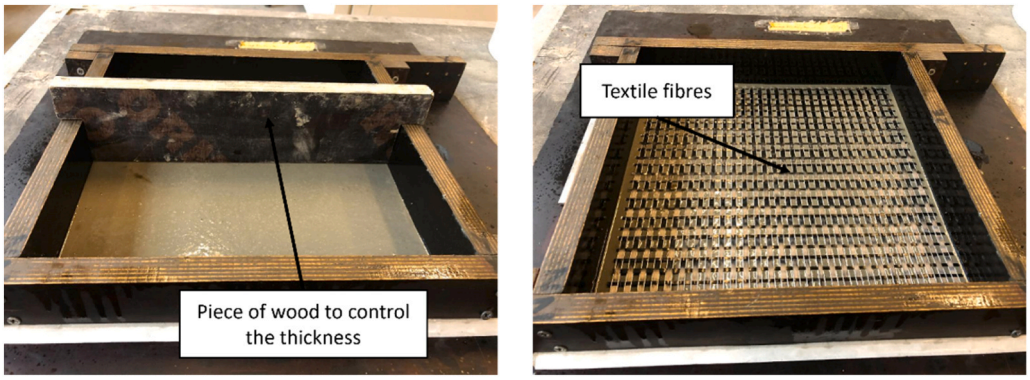

Fig. 5. Construction of TRC panels.

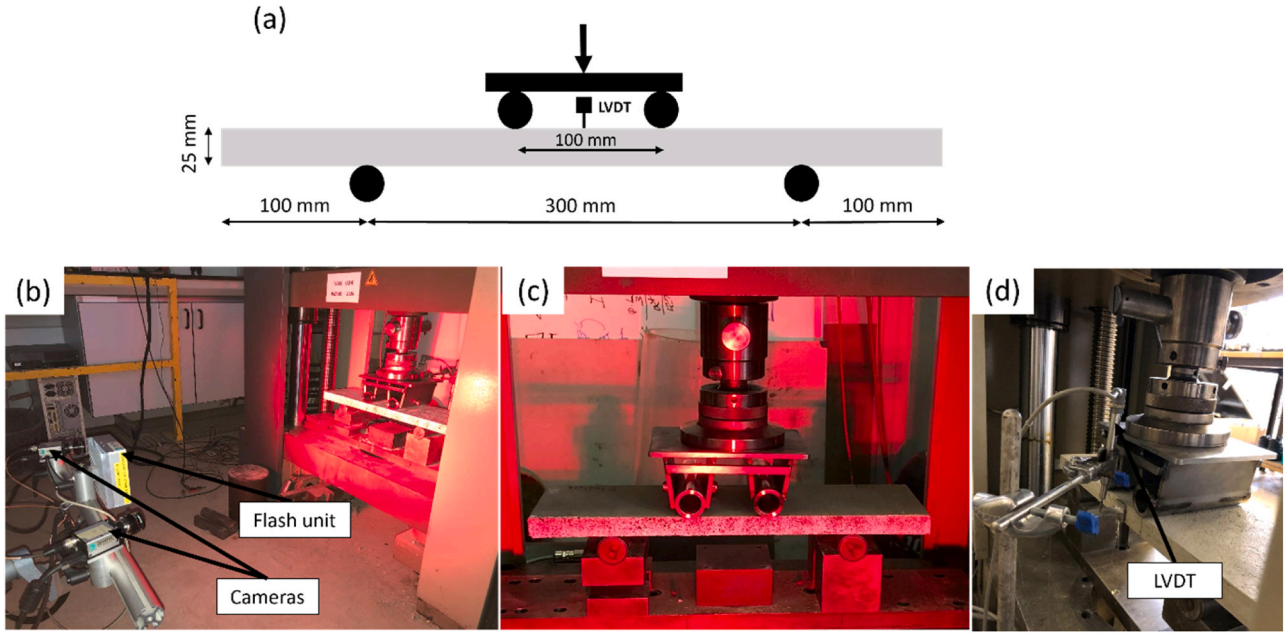

Fig. 6. (a) Schematic view of four-point bending test, (b) DIC system, (c) Four-point bending test setup, (d) Setup of LVDT.

× 25 mm (Fig. 4), while those used for the panel specimens had dimensions of 280 mm × 280 mm × 25 mm (Fig. 5). The initial step involved filling a mortar layer with a thickness of 5 mm, followed by laying and then carefully pressing the first layer of the textile onto the surface of the mortar, as illustrated in Figs. 4 and 5. Once this had been completed, three more layers were laid in sequence, which comprised another layer of mortar with a thickness of 15 mm, a second textile fibre layer, and third layer of mortar with a thickness of 5 mm to fill the remaining volume of the formwork. This was followed by peeling off the specimen surface, thus revealing a smooth surface plane underneath. To ensure that the surface did not dry out or shrink subsequent to being cast, a polyethylene film was applied to cover the specimens. After being

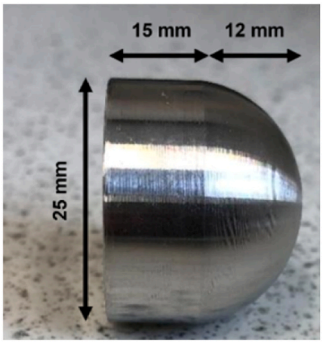

Fig. 7. Hemispherical steel projectile used for impact test.

demoulded, the specimens were stored in a curing room for 24 hrs at a temperature of 20 °C. All specimens were then tested between 28 and 30 days after being fabricated. As a reference, plain concrete panels (containing and not containing steel fibres) that had been produced.

2.4. Test setups and instrumentation

2.4.1. Four-point bending tests

For each beam configuration, three identical specimens were prepared. A four-point bending test was conducted using a Zwick machine by controlling a constant displacement of 1 mm/min. The specimens were placed with a clear span of 300 mm and 100 mm between the two-point load (Fig. 6a).

The load was measured using a load cell and the midspan deflection was determined using LVDT supported on an L-shaped knife edge, which was glued at the midspan top face of each specimen (Fig. 6c and d). Crack formation and midspan deflection were also monitored optically and evaluated using digital image correlation (DIC), as shown in Fig. 6b. High-resolution DIC images were acquired using a Canon camera at 5 s intervals during the load process. The overall time of the test ranged between 55 s and 780 s, depending on the type of specimen being tested. DIC assessment was performed using Istra 4D software. The midspan deflection was calculated for each specimen in the DIC images by tracking a point at the midspan vertically on the analysed surface, as proposed in [39].

2.4.2. High-velocity impact load

High-velocity projectile impact testing of concrete panels was conducted with different impact velocities to investigate the impact resistance and failure mode of each group of concrete specimens. Although

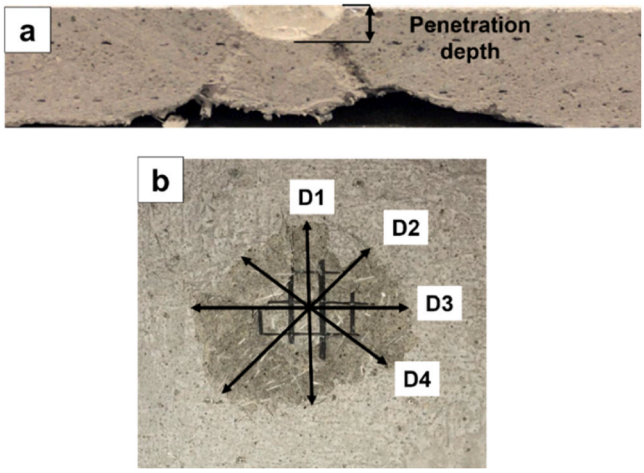

Fig. 9. Measurement of the key parameters after impact loading test, (a) Penetration depth, (b) Average scabbing diameter.

no standards exist to describe the procedure for evaluating the impact resistance, two main methods are used both aiming to increase the kinetic energy. The projectile's velocity can be increased by compressed air pressure or by raising the projectile's mass to enhance kinetic energy. Fig. 8 illustrates the first approach, used in this study. The projectile was manufactured using maraging steel (M−300), with a hemispherical front measuring 25 mm in diameter and 68 g in weight (Fig. 7).

According to [34,36], the range of the high velocity of the projectile that can cause local damage to concrete targets and meet the assumption of a rigid projectile is between 10 m/s to 1000 m/s. In this study, the projectile speed ranged between ~60 and ~160 m.s^{-1}. However, to simplify, the selected velocities were categorised into three categories: low (60–90 m.s^{-1}), medium (80–120 m.s^{-1}), and high (90–160 m.s^{-1}).

The firing system is composed by a highly pressurised tank and a 3.5 m-long gun barrel into a closed 90 ×90 x 90 cm^3 impact chamber. The impact chamber was encased with polycarbonate to guarantee that fragments of both the concrete and the projectile would be confined to the chamber upon impact. A 25 kg sandbag wrapped in Kevlar and further polycarbonate shielding was placed behind the panel to ensure that if the target sample was penetrated, the projectile and produced debris was contained.

The tested specimens were placed vertically in the target chamber, with strong tape holding their top and bottom edges in the centre of the chamber. The velocity of the projectile was changed by changing the

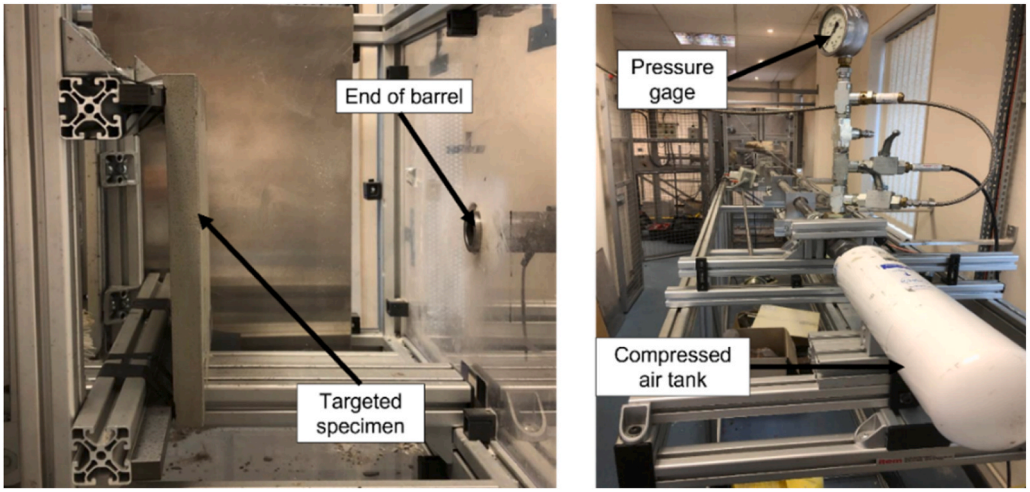

Fig. 8. The experimental test setup for the impact loading test.

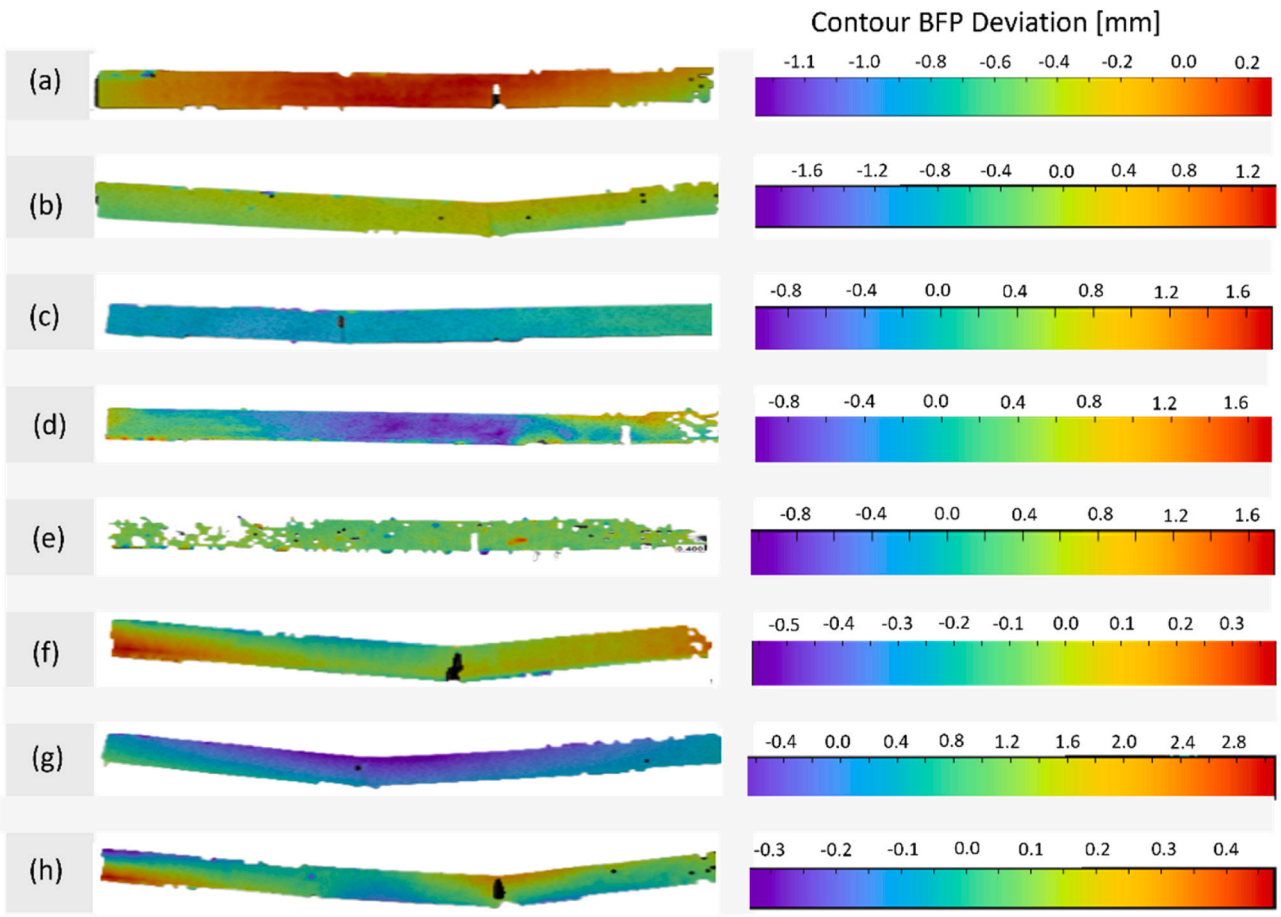

Fig. 10. Modes of failure of plain and TRC beams under four-point bending test: (a) B-M1, (b) B-M1-G, (c) B-M1-C, (d) B-M2-G, (e) B-M2-C, (f) B-UHP, (g) B-UHP-C, (h) B-UHP-G. (Note: Due to the sudden failure of B-M1, DIC could not capture the failure mod).

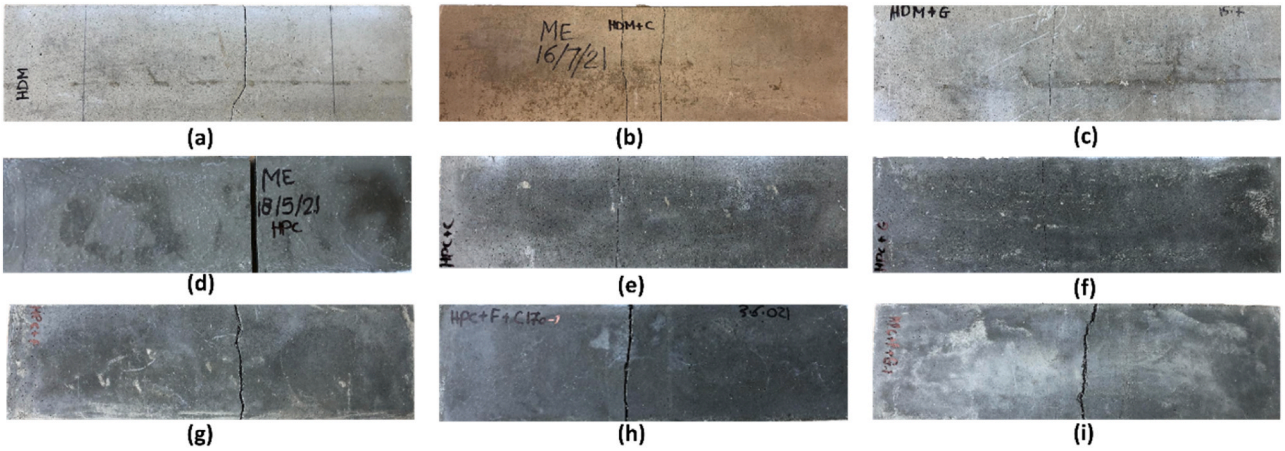

Fig. 11. Crack patterns of plain and TRC beams under four-point bending test; (a) B-M1, (b) B-M1-C, (c) B-M1-G, (d) B-M2, (e) B-M2-C, (f) B-M2-G, (g) B-UHP, (h) B-UHP-C, (i) B-UHP-G.

vessel pressure, while a digital storage oscilloscope equipped with a pair of laser gates situated 100 mm apart was used for velocity measurement, where the two lasers intersected the barrel of the gun. Additionally, translation of the signals for the data processor in the oscilloscope was performed by a pair of receivers.(Fig. 8)

A high-speed camera (Phantom V12.1) with a maximum frame rate of 14,000 per second was placed at the edge of the target chamber for the purpose of measuring the projectiles' initial velocity and observing how the tested panels deformed in every test. Subsequent to each impact test, measurements were taken of the depth of penetration and average scabbing diameter, as illustrated in Fig. 9.

3. Test results and discussion

3.1. Four-point bending test results

3.1.1. Failure modes

As presented in Figs. 10 and 11, DIC was used to monitor the crack

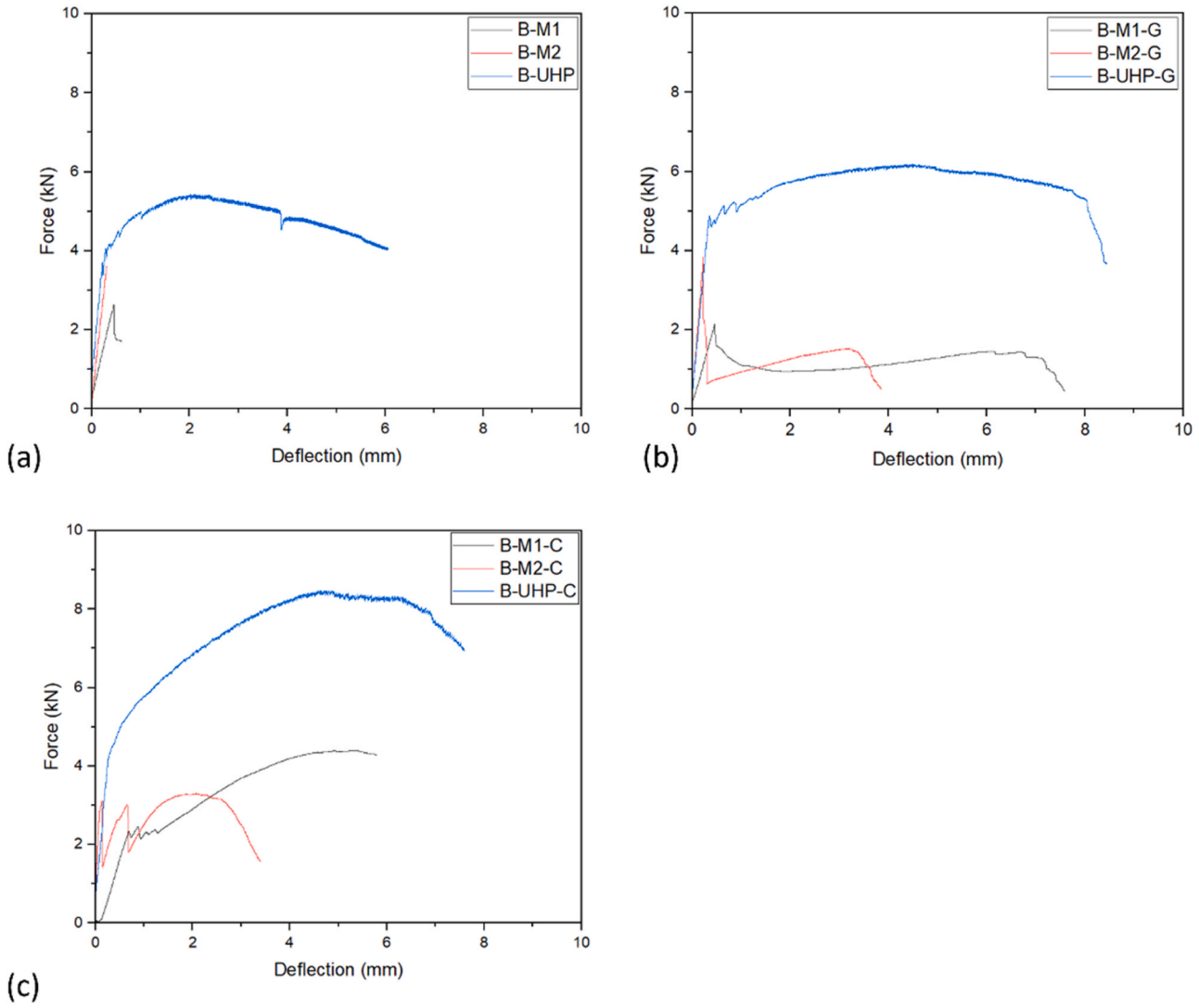

Fig. 12. The average Load – deflection curves: (a) non-reinforced textile fibre specimens, (b) glass textile fibre reinforced specimens, (c) carbon textile fibre reinforced specimens.

pattern, vertical displacement, and failure mode of the beams being tested under flexural load. As can be observed in the figures, the TRC specimens had failure modes featuring the development of longitudinal straight continuous cracks across the matrix-textile interface, which spread as the load increased (Fig. 11 b, c, e, f). Specimens in which fibres were contained exhibited irregular cracks, and the crack propagation was considerably restrained by the bridging effect of the steel fibres. However, this behaviour was only observed until reaching a certain limit (approximately 70–80 % of the peak load), at which point the cracks at the bottom of the samples began to expand. This occurred because the steel fibres, which acted as bridges across the gaps, were pulled out as the cracks widened (Fig. 10 f, g, h). Finally, the control specimens (M1 and M2) were failed due to the collapse of the mortars.

3.1.2. Load-deflection response

The load versus midspan deflection curves for all the tested rectangular TRC beams are shown in Fig. 12. The high compressive strength mixture (M2, Fig. 12a) presented a higher first-cracking strength and greater flexural strength than the M1 mortar. The midspan deflection for the M1 specimens in all cases "B-M1, B-M1-G, B-M1-C" was higher than that in the M2 specimens "B-M2, B-M2-G, B-M2-C". For the control specimens "B-M1, B-M2", after achieving the ultimate flexural load, the softening behaviour of the B-M1 specimens was similar to the hardening behaviour, whereas a sudden load drop with local failure was recorded for the B-M2 specimens.

The flexural capacity of the mortars significantly improved with the addition of textiles: in the post-cracking stage, as the flexural load increased (Fig. 12b, and c) the cracks propagated upwards, and the width of the crack increased. Therefore, the tension force at the cracks was borne by the textile and the section stiffness was improved due to the contribution of the textiles. Although both mortars (M1 and M2) reinforced with glass and carbon textiles showed hardening behaviour after the initial cracking, the overall flexural behaviour of both mortars was quite different under a static flexural load. In comparison with carbon textile, the M1 and M2 mortars reinforced with glass textile showed a sudden drop in load after the initial cracking, which may be attributable to the structure of the glass textile. The flexural strength and midspan deflection of UHP specimens was significantly improved due to the bridge effect of steel fibres, where fibres spanning across the cracks that develop under loading to act as reinforcement, preventing further crack propagation and enhancing the overall toughness of the material.

Table 5 presents the ultimate flexural load, midspan deflection, and toughness of all tested beams. Toughness quantifies the energy absorption capability of the TRC specimens during plastic deformation and it was calculated as the area under the load–deflection curve as proposed in [40]. Therefore, it depends on the deflection that corresponds to the

Table 5
Average values of the ultimate load and corresponding deflection, and flexural toughness.

Specimen ID	Average value (STD)		
	Ultimate load kN	Ultimate deflection mm	Flexural toughness N.mm x10^3
B-M1	2.64 (0.112)	0.45 (0.098)	0.60 (0.135)
B-M1-C	4.40 (0.175)	5.34 (0.877)	19.03 (1.413)
B-M1-G	2.14 (0.116)	6.67 (0.084)	8.30 (0.941)
B-M2	3.62 (1.261)	0.31 (0.078)	0.51 (0.810)
B-M2-C	3.30 (0.158)	2.07 (0.127)	5.59 (0.811)
B-M2-G	3.84 (0.120)	3.41 (0.605)	4.31 (1.025)
B-UHP	5.43 (1.887)	2.02 (1.206)	9.27 (2.031)
B- UHP-C	8.48 (0.672)	4.60 (1.054)	31.02 (3.586)
B- UHP-G	6.184 (0.293)	5.48 (0.418)	24.54 (3.014)

*STD: Standard Deviation

material failure.

The first cracking load of M2 specimens reinforced with glass and carbon textiles "B-M2-G, B-M2-C respectively" is higher than that in the "B-M1-G, B-M1-C" by 44 % and 24 % respectively, and this is due to the high compressive strength of M2 mixture. However, the ultimate flexural strength of B-M1-C was 25 % higher than that of B-M2-C and the ultimate flexural strength for M1 and M2 mortars reinforced with glass textile was almost the same. In comparison with the pre-cracking stage, the slope of the curve in the post-cracking stage for B-M1-G, and B-M2-G decreased, which indicates that the flexural stiffness of the cracked TRC specimen reinforced with glass textile was reduced. The midspan deflection for B-M1-G and B-M1-C is higher than that for B-M2-G and B-M2-C by 49 % and 61 %, respectively, which can be attribute to the higher ductility of M1.

For UHP specimens, the flexural strength of B-UHP was 5.43 MPa, which was 33 % higher of that for the B-M2. This outcome is attributable to the flexural strength of the composite increasing as the compressive strength increases and the fibres also resist the tensile stresses. For UHP specimens reinforced with carbon and glass textiles "B-UHP-C, and B-UHP-G" the flexural strength and midspan deflection were significantly increased and this reflected the increase in flexural toughness.

As expected, the crack resistance and the first-crack flexural load of the mortar were increased as a result of adding steel fibres to the mortar. Moreover, the performance of the interfacial bonding between the textile and mortar was improved as a result of the steel fibres integrated into the textile grids, resulting in improved flexural load and toughness.

3.2. *Impact loading test results*

3.2.1. *Observed behaviour*

Figs. 13, 14, and 15 present the damage caused on each sample under different high-velocity projectile impact load. The failure modes of the tested panels are classified as: penetration, scabbing, cracks on the front face and/or back face, and perforation. Despite the failure mode depending on the mechanical properties of the cementitious matrix and the type of reinforcement, the specimens show a combination of failure modes, including perforation or penetration with spalling as well as scabbing and perforation with scabbing and cracks on the back face.

The plain M1 panels showed perforation with cracks on the back face

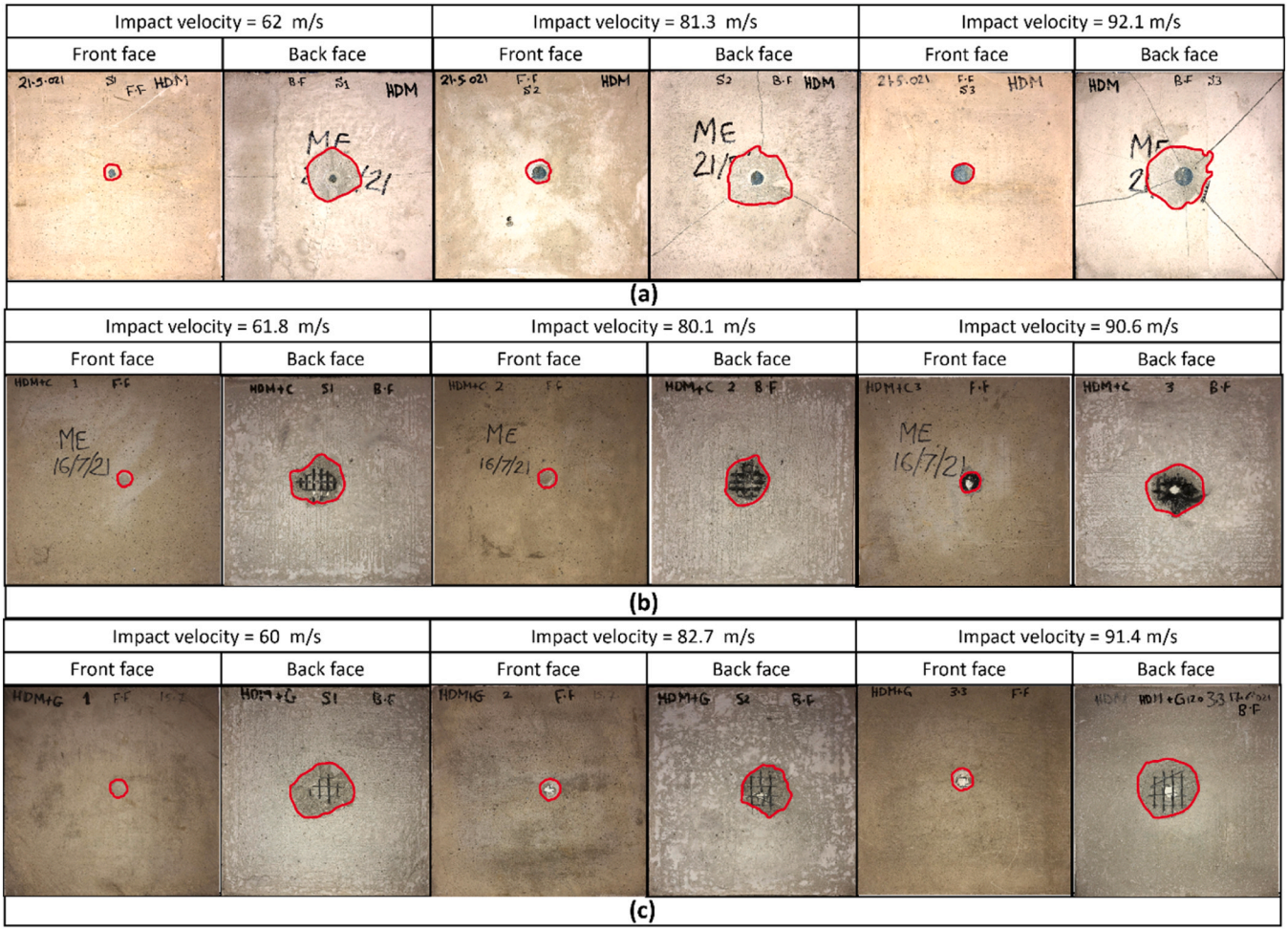

Fig. 13. Failure modes of panels after the impact test: (a) P-M1, (b) P-M1-C, (c) P-M1-G.

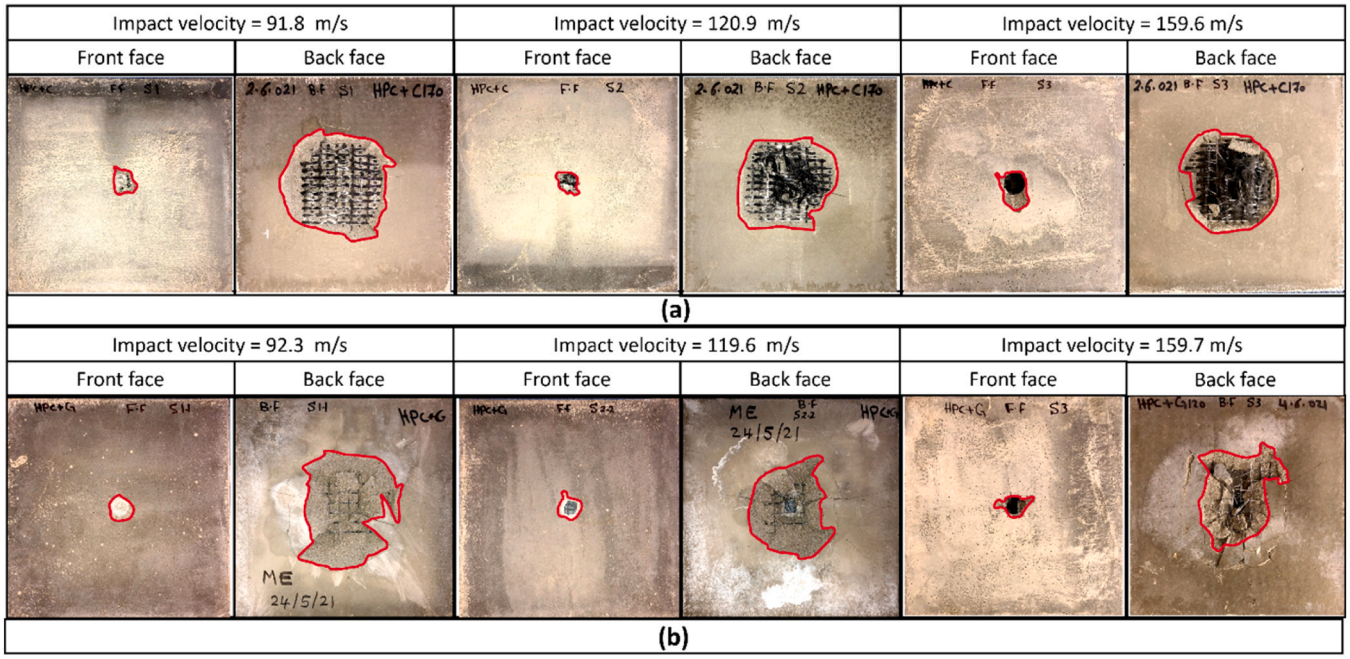

Fig. 14. Failure modes of panels after the impact test: (a) P-M2-C, (b) P-M2-G. Note: P-M2 was broken into pieces.

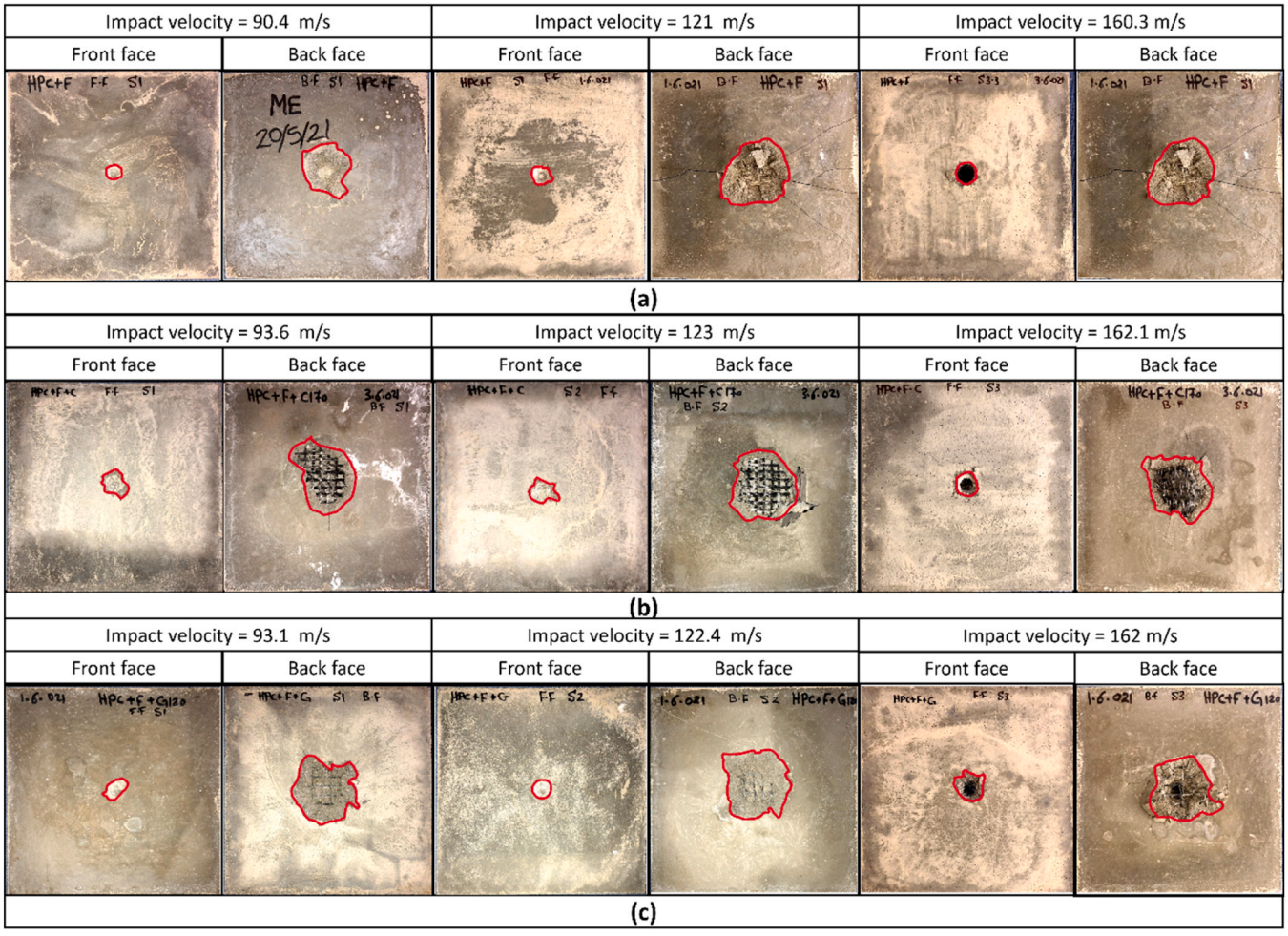

Fig. 15. Failure modes of panels after the impact test: (a) P-UHP, (b) P-UHP-C, (c) P-UHP-G.

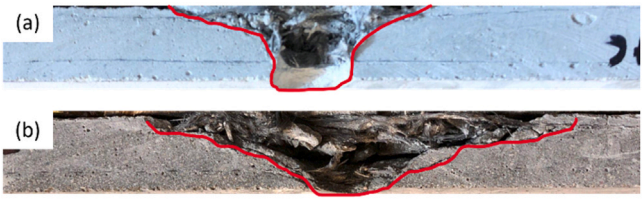

Fig. 16. Cross-section of tested panels shows damage caused by high-velocity impact load, (a) P-M1-C, (b) P-M2-C.

Table 6
Test results of high-velocity impact loading tests.

Specimens ID	V_0 (m/s)	Failure mode	P_d (mm)	S_d (mm)	M_l(%)
P-M1-*l*	62.0	Perforation with scabbing and back face cracks	>25	71	1.79
P-M1-*m*	81.3	Perforation with scabbing and back face cracks	>25	80	3.13
P-M1-*h*	92.1	Perforation with scabbing and back face cracks	>25	87	4.03
P-M1-C-*l*	61.8	Penetration with scabbing	6	67	1.74
P-M1-C-*m*	80.1	Penetration with scabbing	14	69	1.87
P-M1-C-*h*	90.6	Perforation with scabbing	>25	74	2.53
P-M1-G-*l*	60.0	Penetration with scabbing	8	74	1.86
P-M1-G-*m*	82.7	Perforation with scabbing	>25	76	1.92
P-M1-G-*h*	91.4	Perforation with scabbing	>25	82	2.07
P-M2-*l*	62.4	Perforation*	>25	-	-
P-M2-*m*	82.0	Perforation*	>25	-	-
P-M2-*h*	90.6	Perforation*	>25	-	-
P-M2-C-*l*	91.8	Penetration with scabbing	6	135	3.21
P-M2-C-*m*	120.9	Perforation with scabbing	>25	130	4.48
P-M2-C-*h*	159.6	Perforation with scabbing	>25	125	5.09
P-M2-G-*l*	92.3	Penetration with scabbing	7	140	2.34
P-M2-G-*m*	119.6	Perforation	>25	136	2.92
P-M2-G-*h*	159.7	Perforation	>25	134	3.15
P-UHPFRCC-*l*	90.4	Penetration with scabbing	7	81	1.24
P-UHPFRCC-*m*	121.0	Penetration with scabbing and cracks**	10	81	1.59
P-UHPFRCC -*h*	160.3	Perforation with scabbing and cracks**	>25	83	2.25
P-UHPFRCC -C-*l*	93.6	Penetration with scabbing	6	82	0.91
P-UHPFRCC -C-*m*	123.0	Penetration with scabbing	9	94	0.94
P-UHPFRCC -C-*h*	162.0	Penetration with scabbing	20	82	1.03
P-UHPFRCC -G-*l*	93.1	Penetration with scabbing	8	88	1
P-UHPFRCC -G-*m*	122.4	Penetration with scabbing	9	89	1.31
P-UHPFRCC -G-*h*	162.0	Perforation	>25	86	1.78

Note: V_0 is the projectile velocity, P_d is the penetration depth, S_d is the scabbing diameter, M_l is the mass loss, *Broken into pieces, ** Cracks at the back face.

(Fig. 13a), whereas the plain M2 panels were perforated and had broken into pieces. This can be explained by the fact that M2 has high compressive strength, as well as how it effects the penetration strength;

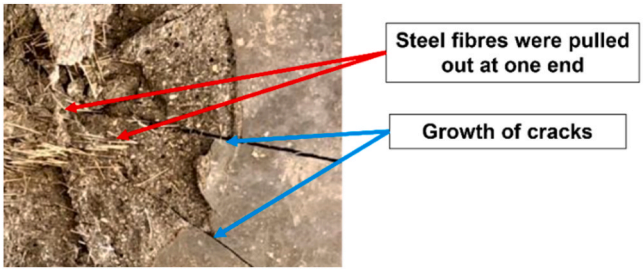

Fig. 17. Fibre fracture shape on the rear face following an impact test.

nevertheless, this did not stop cracks from propagating when the impact occurred as a result of the material's brittleness. Although the control M1 panels had comparatively low compressive strength, the reason they were more resistant to crack propagation, which could result in the specimens failing completely, was probably their increased toughness and flexural capacity as presented in Table 5. The impact resistance for M1 and M2 panels reinforced with carbon textile "P-M1-C and P-M2-C" and glass textile fibres "P-M1-G and P-M2-G" was improved relative to penetration depth and scabbing diameter, and the panels showed penetration with scabbing at lower velocities "60 and 90 m.s-1" (Fig. 13b, and c). It was observed that the mass loss of the M1 panels reinforced with carbon "P-M1-C" and glass textile "P-M1-G" was lower than that of the M2 panels "P-M2-C, P-M2-G" tested with an identical condition (Fig. 16) by 26.8 % and 13.04 % respectively. The average crater diameters of M1 panels reinforced with carbon (Fig. 13b) and glass textile (Fig. 13c) was also lower than that of the M2 panels reinforced with the same materials (Fig. 14a, and b) and this is attributable to a highly ductility of the composite as presented in the four-point bending test results, such as the M1 mortar, absorbed external energy through high deformation that resulted in microcracks. Given identical test conditions, it can be concluded that the effective region, in which high-velocity impact loads have a direct impact, of the M2 panels is larger than that of the M1 panels.

The failure mode for P-UHP-*l* and P-UHP-*m* was penetration with scabbing and cracks on the back face (Fig. 15a). Perforation with scabbing was also observed for other panels "P-M1-C-*h*, P-M1-G-*m* and P-M1-G-*h*" "Fig. 13b, and c".

While the M1 and M2 panels reinforced with carbon and glass textile reinforcement exhibited three stages at lower velocities (impact cratering, tunnelling, and rear shear plugging), there was no perforation, while any damage was minimal and limited to particular areas. This is attributable to the textile fibres bridging the cracks and increasing the tensile strength and flexural capacity, indicating that the use of textile fibres can enhance the performance of scabbing resistance. Further observation revealed that when perforation occurred, the damaged area at the front face was smaller than that at the back face, and this is the typical failure mode of reinforced concrete following a projectile impact load [41–43].

3.2.2. *Impact resistance performance*

As presented in Table 6, the use of textiles with fibres has significantly improved impact resistance and decreased spalling, scabbing, and damage size, as well as improved energy absorption capacity, in comparison to UHP panels. The mass losses at a velocity of 160 m.s^{-1} for P-UHP-C and P-UHP-G were 80 % and 44 % lower than those for the P-M2-C and P-M2-G respectively. The steel fibres that bridged the cracks were pulled out due to the impact load, resulting in an increase of the crack width (Fig. 17). The improvement in flexural toughness resulted in the dissipation of energy when extracting the steel fibres, simultaneously, the steel fibres served to carry the tensile stress from the cracked mortar, therefore enhancing the impact resistance of the panels. Furthermore, the inclusion of steel fibres in the textile grids effectively prevented any movement between the textiles and the mortar due to the anchoring

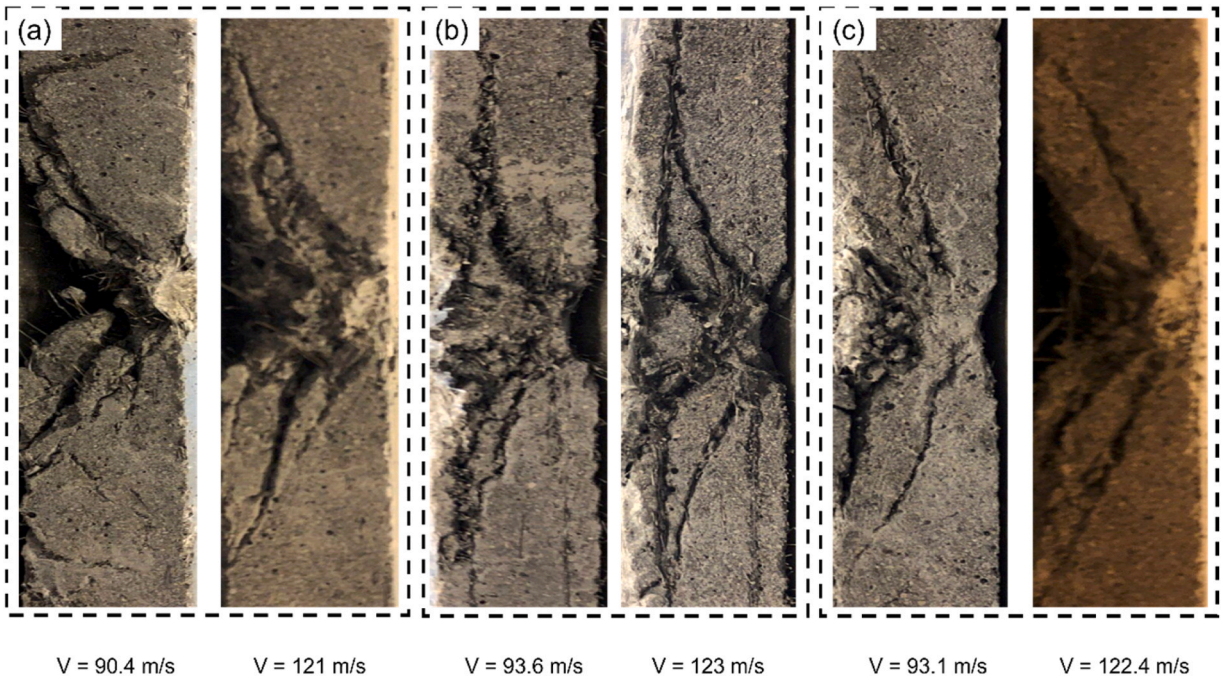

Fig. 18. Cross-section of tested panels: (a) P-UHP, (b) P-UHP-C, (c) P-UHP-G.

Table 7
Empirical formulas for the prediction of penetration depth.

Model name	Expression	Nose shape factor	Application range
Modified Petry [46]	$\frac{x}{d}=K\left(\frac{M}{d^3}\right)\log10(1+\frac{V^2}{19,974})$ K=6.36×10^{-4} for plain concrete, 3.39×10^{-4} for normal reinforced concrete, 2.26×10^{-4} for specially reinforced concrete	NA	NA
Ballistic Research Laboratory (BRL) [47]	$\frac{x}{d}=\frac{1.33\times10^{-3}}{\sqrt{f_c}}\left(\frac{M}{d^3}\right)d^{0.2}V^{1.33}$	NA	NA
Whiffen [48]	$\frac{x}{d}=\frac{2.61}{\sqrt{f_c}}\left(\frac{M}{d^3}\right)\left(\frac{d}{a}\right)^{0.1}\left(\frac{V}{533.4}\right)^{n};\ n=\left(\frac{97.51}{f_c^{0.25}}\right)$	NA	5.52<f_c<68.95; 0.136<M<9979.2 12.7<d<965.2; 0<V<1127.8h
US Army Corps of Engineers (ACE) [49]	$\frac{x}{d}=\frac{3.5\times10^{-4}}{\sqrt{f_c}}\left(\frac{M}{d^3}\right)d^{0.215}V^{1.5}+0.5$	NA	NA
Modified National Defence Research Committee (NDRC) [50]	$G=3.8\times10^{-5}\frac{N\times M}{d\sqrt{f_c}}\left(\frac{V}{d}\right)^{1.8}\quad\frac{x}{d}=\begin{cases}2G^{0.5} & \text{ifG}\geq1\\ G+1 & \text{ifG}<1\end{cases}$	N = 0.72 flat; 0.84 blunt; 1.00 spherical; 1.14 sharp	NA
Ammann and Whitney [51]	$\frac{x}{d}=\frac{6\times10^{-4}}{\sqrt{f_c}}N\left(\frac{M}{d^3}\right)d^{0.2}V^{1.8}$	N = 0.72 flat; 0.84 blunt; 1.00 spherical; 1.14 sharp	Small fragment V >300
Kar [52]	$G=3.8\times10^{-5}\left(\frac{E}{E_s}\right)^{1.25}\frac{N\times M}{d\sqrt{f_c}}\left(\frac{V}{d}\right)^{1.8}$ For G≥1 $\frac{x}{d}=2G^{0.5}$ For G<1 $\frac{x}{d}=G+1$	N = 0.72 flat; 0.84 blunt; 1.00 spherical; 1.14 sharp	NA
Hughes [53]	$\frac{x}{d}=0.19\left(\frac{N\times Ih}{S}\right);\ Ih=\frac{M\times V^2}{d^3\times f_t};\ S=1+12.3\ln(1+0.03Ih)$	N = 1 flat; 1.12 blunt; 1.26 spherical; 1.39 sharp	Ih < 3500
Haldar–Hamieh [54]	$\boldsymbol{Ia=\frac{N\times M\times V^2}{d^3\times f_c}}$ For $0.3\leq Ia\leq4$ $\boldsymbol{\frac{x}{d}=-0.0308+0.2251Ia}$ For $4<Ia\leq21$ $\boldsymbol{\frac{x}{d}=0.674+0.0567Ia}$ For $21<Ia\leq455$ $\boldsymbol{\frac{x}{d}=1.1875+0.0299Ia}$	N = 1 flat; 1.12 blunt; 1.26 spherical; 1.39 sharp	NA
Adeli–Amin [55]	$Ia=\frac{N\times M\times V^2}{d^3\times f_c}$ For $0.3<Ia<4$ $\frac{x}{d}=0.0416+0.1698Ia-0.0045Ia^2$ For $4\leq Ia<21$ $\frac{x}{d}=0.0123+0.196Ia-0.008Ia^2+0.0001Ia^3$	N = 1 flat; 1.12 blunt; 1.26 spherical; 1.39 sharp	0.11<M<343; d≤ 0.3; 27<V<312
Healey and Weissman [56]	$G=4.36\times10^{-5}\left(\frac{E}{E_s}\right)\frac{N\times M}{d\sqrt{f_c}}\left(\frac{V}{d}\right)^{1.8}\quad\frac{x}{d}=\begin{cases}2G^{0.5} & \text{ifG}\geq1\\ G+1 & \text{ifG}<1\end{cases}$	N = 1 flat; 1.12 blunt; 1.26 spherical; 1.39 sharp	NA
The United Kingdom Atomic Energy Authority (UKAEA) [57]	$G=3.8\times10^{-5}\frac{N\times M}{d\sqrt{f_c}}\left(\frac{V}{d}\right)^{1.8}$ For G≤0.0726 $\frac{x}{d}=0.275-[0.0756-G]^{0.5}$ For 0.0726 ≤G≤ 1.0605 $\frac{x}{d}=[4G-0.242]^{0.5}$ For G≥ 1.0605 $\frac{x}{d}=G+0.9395$	N = 1 flat; 1.12 blunt; 1.26 spherical; 1.39 sharp	22< f_c <44; 5000<M/d<20000; 25<V<300
The IRS [58]	$x=3703.376f_c^{-0.5}+82.152f_c^{-0.18}\exp[0.104f_c^{-0.18}]$	NA	NA

Note: G is the impact function, x is the penetration depth (m), a is the aggregate size, d is the diameter of projectile (m),), Ih, Ia is the impact factor, S is the dynamic increase factor, N is the nose shape factor of projectile, M is the mass of projectile (Kg), V is the velocity of projectile (m/s), f_c is the compressive strength of concrete (N/m^2), f_t is the tensile strength of concrete (N/m^2), E is the Young's modules of projectile (N/m^2), E_s is the Young's modules of steel (N/m^2)

Table 8
Performance of empirical models.

Model	STD*	COV**
Modified Petry [46]	0.73	0.59
BRL [47]	0.13	4.89
US (ACE) [49]	0.31	2.66
NDRC [50]	1.35	0.52
Kar [52]	1.35	0.44
Haldar–Hamieh [54]	0.08	6.38
Healey and Weissman [56]	0.52	1.05
IRS [58]	0.44	2.42

*STD: Standard Deviation, **COV: Coefficient of Variation

effect, leading to an enhanced bonding performance at the interface between the mortar and textiles. Enhanced interfacial bonding performance has the potential to provide optimal collaboration between the mortar and the textile, hence improving the usage of the tensile strength of textiles. As a result, the impact resistance of the UHP panels reinforced with textile was improved, particularly for the P-UHP-C panels.

The best impact resistance performance was observed for the UHP specimens reinforced with carbon textile "P-UHP-C". As presented in Table 6, the depth of penetration for P-UHP-C at an impact velocity of 162 m.s^{-1} was 20 mm, whereas P-UHP and P-UHP-G were fully perforated at the same impact velocity. However, at lower velocities, the influence of the inclusion of UHP with textile fibres was limited, since the depth of penetration for P-UHP-C, P-UHP, and P-UHP-G specimens was almost the same "6, 8, 7 mm respectively" for impact velocity of 90 m/s and 9, 10, 9 mm for impact velocity of 120 m.s^{-1}.

When textile fibres were used to reinforce both the impact and back face of the TRC panels, the tensile strength was considerably improved. This resulted in them being resistant to the high tensile stress waves that manifested in the panels' back face caused by the reflection of compressive stress waves due to the impact of the projectile. Due to the TRC material being highly ductile, it was capable of tolerating the increased magnitude of the tensile stress waves, while also enabling the wave energy to be dampened, and offering further mechanisms for resisting impact as a result of its membrane behaviour and ability to distribute the stress of the impact across a wider impact zone.

To further comprehend the crater damage and crack propagation of the panels that underwent high-velocity impact load testing, each panel was cut into two equal parts at the impact point. As demonstrated by the comparison between crack patterns presented in Fig. 18, it is evident that reinforcing the concrete with textiles (Fig. 18b and c) resulted in improved resistance to impact and stopped smash failure from occurring by limiting the propagation of cracks, thus lowering any secondary damage caused by the scabbing and spalling fragments and restricting the internal local impact position, whereas multiple radial cracks emerged on the back face, as well as minor cracks on the side surface of the UHP panels as a result of the projectile penetrating. In general, while the findings are not conclusive, incorporating textile fibres can more effectively reduce the penetration depth, while also restricting crack propagation at the panels' distal face, thus limiting the size of scabbing or crater areas. Fig. 18c also shows a delamination failure of specimens that incorporated glass textiles, which could be attributed to the bond strength between the glass and the cementitious matrix.

Overall, it was found that the P-UHP-C panels had greater resistance to high-velocity projectile impact loads than the other specimens in terms of depth of penetration, crater diameter, and mass loss. However, the variation in impact resistance capacities between M2 and M1 mortars is not as clear as the difference in compressive strengths "100 MPa for the M2 mortar and 29 MPa for the M1 mortar, respectively".

4. Assessment of analysis models

Numerous existing design guidelines [44,45] advise using empirical expressions to assess the penetration depth of concrete panels under high-velocity impact loads. The most widely used empirical expressions [46–58] are presented in Table 7. The nose shape factor and range of application for each model is also included in Table 7.(Table 8)

The empirical formulas presented in Table 7 were utilised to estimate the predicted penetration depth (PPD) and compared with the experimental value of the penetration depth (EPD) as shown in Fig. 19. It is noted that due to restrictions related to the application range of the expressions in Table 7 (i.e., the models were developed by data fitting of experimental test results corresponding to a specific range of parameters), only Modified Petry [46], BRL [47], US (ACE) [49], NDRC [50], Kar [52], Haldar-Hamieh [54], Healey and Weissman [56], and IRS [58] models have been analysed.

The accuracy of the different models in predicting the values of penetration depth were assessed by the standard deviation (STD) and coefficient of variation (COV) as [59,60]:

$$SD = \sqrt{\frac{\sum_{i=1}^{n}\left(\frac{p_i^a - M^a}{p_i^e - M^e}\right)^2}{N-1}} \quad (1)$$

$$COV = \sqrt{\frac{\sum_{i=1}^{n}\left(\frac{p_i^e}{p_i^a} - 1\right)^2}{N}} \quad (2)$$

where p_i^a, and p_i^e are the predicted and the experimental penetration depth respectively. M^a, and M^e are the mean predicted and observed penetration depth.

As observed in Fig. 19, the penetration depth of the control panels (P-M1, P-M2) has been underestimated by all the expressions and the most accurate expressions were Kar [52] and Healey and Weissman [56]. In this paper, it was found that the increase in compressive strength did not lead to a reduction in penetration depth. Both plain panels (M1 and M2) were fully perforated during the test. However, the penetration depth calculated using empirical formulas for M2 was lower compared to M1. This could be attributed to the empirical expressions not taking into account the thickness of the panels. For TRC panels "P-M1-C, P-M1-G, P-M2-C, P-M2-G", a huge variation in the calculated penetration depth was observed. For instance, the ACE [49], Kar [52], Healey and Weissman [56] expressions overestimated the penetration depth, on the other hand the Haldar–Hamieh [54], BRL [47], and IRS [58] expressions underestimated the PPD. The NDRC [50] and the modified Petry [46] expressions have yielded the smallest COV = 0.52, and 0.59 respectively.

Nevertheless, the depth of penetration of the projectile was significantly impacted by the volume and type of reinforcement employed [36]. For example, when fibres are integrated into concrete, both its tensile strength and toughness can be improved, resulting in the performance under impact loading being superior to conventional concrete as a result of the ability to limit cracks, thus reducing the area subject to damage. Nevertheless, the tested expressions do not consider how reinforcement affects the penetration depth apart from the modified Petry model [46] in which a K factor that represents the penetrability of concrete according to the degree of reinforcement and strength of the concrete is incorporated. Similar to standard reinforced concrete, the factor

remained constant "3.39×10^{-4}". This factor does not offer a precise definition for 'specially reinforced concrete' or specifically consider the type and volume of reinforcement, as the majority of empirical models concentrate on the behaviour of conventional plain concrete.

From the above analysis, and to the best of the authors knowledge, there is no empirical expression to predict the penetration depth for TRC panels. Therefore, a numerical analysis is required to better understand the behaviour of TRC panels under high-velocity impact load. This will be a crucial area of research to be explored in future studies, as it has the potential to significantly advance the development and implementation of TRC panels in various applications.

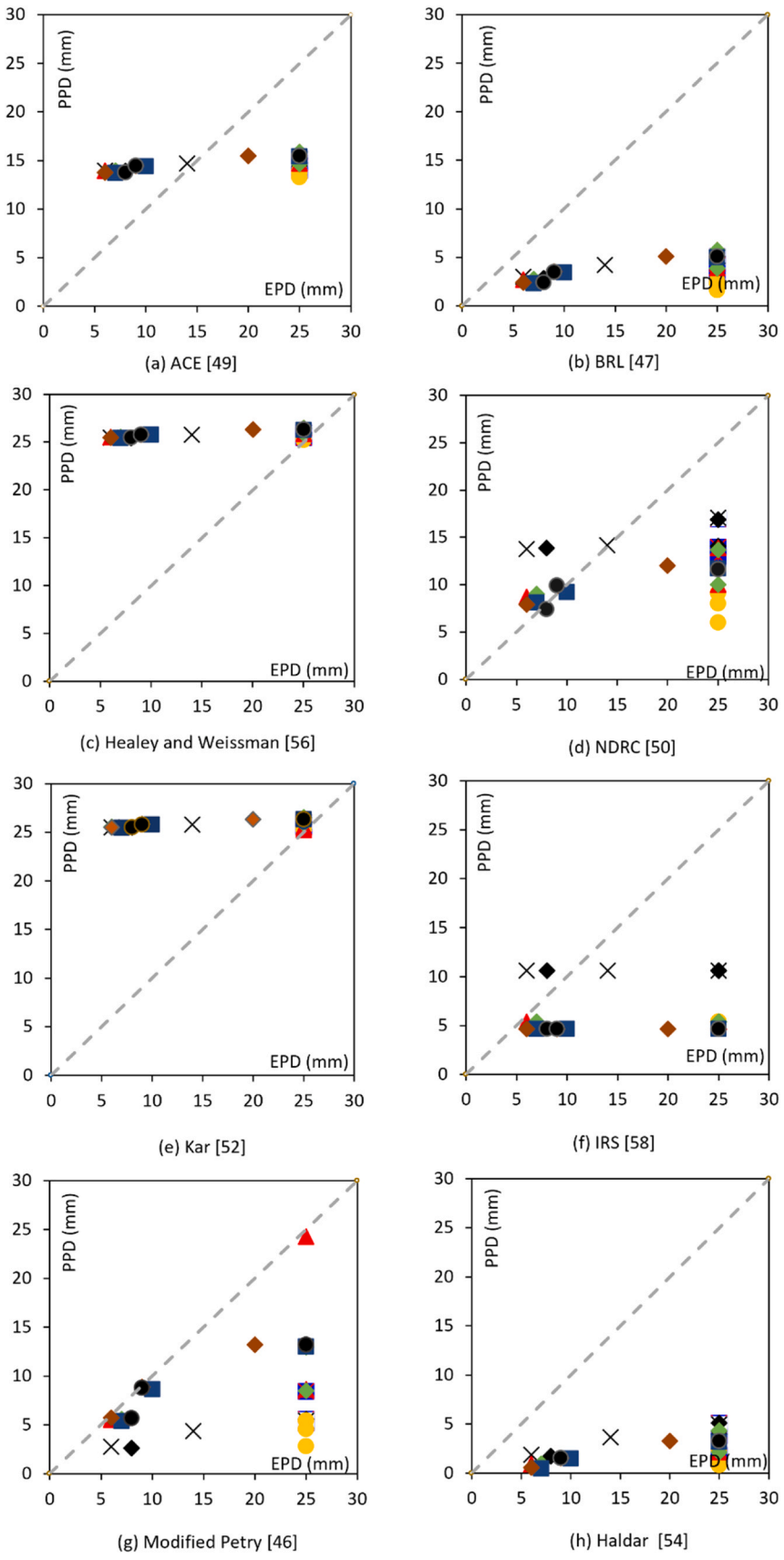

Fig. 19. Predicted Penetration Depth (PPD) VS Experimental Penetration Depth (EPD).

5. Conclusions

This study investigated the potential use of TRC composites to improve the impact resistance of concrete structures. The study involved conducting a series of experiments to examine the mechanical properties and impact resistance of TRC panels. These panels were built using concrete with standard (29 MPa) and high (101 MPa) compressive strength, and were reinforced with carbon, and glass textile. Moreover, a hybrid system combining UHPFRCCs with carbon and glass textile was investigated. Based on the results presented in this paper, the following conclusions can be drawn:

- The results of the four-point bending tests demonstrated that the flexural behaviour of the two types of mortars (M1 and M2) differed significantly, as expected. In all beams, the flexural behaviour of M1 mortar (29.2 MPa) exhibited lower strength and higher flexural ductility compared to M2 mortar (100.6 MPa). However, the use of UHPFRCC with a strength of 132 MPa has significantly enhanced both the flexural and toughness capabilities while also increasing the composite's energy-absorption capacity.
- The results of the high-velocity impact loading tests on control panels indicated that there was no significant variation in impact performance as a result of changing the compressive strength of the concrete.
- The addition of textile fibres significantly enhanced the resistance to impact loading by reducing depth of penetration. In addition, textile-reinforced specimens exhibited localised and reduced damage characterised by negligible spalling and small scabbing and mass loss due to inhibition of crack propagation. In contrast, the use of steel fibres alone caused an irregular distribution of wide cracks that extended from the centre of the impact to the ends of the specimens, which, in extreme cases, led to scabbing as a result of the uneven distribution of fibres during the mix.
- Although the impact resistance of UHPFRCC has generally increased with an improvement in toughness and flexural performance, the use of steel fibres and textiles together generated additional bonding between the mortar and the textile, allowing better use of the tensile strength of the textiles.
- When UHPFRCC and carbon textiles were used, the performance of the panels when subjected to high-velocity impact loading was increased, specifically at higher velocity (160 $m.s^{-1}$). Nevertheless, additional research is required to ascertain how composites can be designed in the most efficient manner with regard to volume fraction and type of fibres that will be employed in protective structures to increase the resistance to impact loading.
- As extant empirical formulas utilised in the prediction of penetration depth relate to conventional concrete, it is necessary to modify them for the purpose of developing new types of materials with increased performance, including the TRC and UHPFRCC types studied in the current research.

CRediT authorship contribution statement

Georgia Thermou: Supervision. **Luis Neves:** Supervision. **Mohamed Esaker:** Writing – original draft, Funding acquisition, Data curation.

Declaration of Competing Interest

The authors declare the following financial interests/personal relationships which may be considered as potential competing interests: Mohamed Esaker reports financial support was provided by University of Nottingham.

Data availability

No data was used for the research described in the article.

Acknowledgements

The first author would like to acknowledge the Libyan Higher Education Ministry for supporting this research. The authors would like to thank MAPEI for providing the mortars and textile fibres used on this research.

References

[1] D. Grote, S. Park, M. Zhou, Dynamic behavior of concrete at high strain rates and pressures: I. experimental characterization, Int. J. Impact Eng. 25 (9) (2001) 869–886.
[2] H. Ueno, M. Beppu, A. Ogawa, A method for evaluating the local failure of short polypropylene fiber-reinforced concrete plates subjected to high-velocity impact with a steel projectile, Int. J. Impact Eng. 105 (2017) 68–79.
[3] H. Kim, et al., Assessment of flexural toughness and impact resistance of bundle-type polyamide fiber-reinforced concrete, Compos. Part B Eng. 78 (2015) 431–446.
[4] S. Wang, et al., Resistance of high-performance fiber-reinforced cement composites against high-velocity projectile impact, Int. J. Impact Eng. 95 (2016) 89–104.
[5] J. Nam, et al., Comparative assessment of failure characteristics on fiber-reinforced cementitious composite panels under high-velocity impact, Compos. Part B Eng. 99 (2016) 84–97.
[6] M. Zhang, et al., Resistance of high-strength concrete to projectile impact, Int. J. Impact Eng. 31 (7) (2005) 825–841.
[7] H.H.Z. Khalel, et al., Parametric study for optimizing fiber-reinforced concrete properties, Struct. Concr. (2024).
[8] H. Khalel, et al., Performance of engineered fibre reinforced concrete (EFRC) under different load regimes: a review, Constr. Build. Mater. 306 (2021) 124692.
[9] R. Yu, P. Spiesz, H. Brouwers, Energy absorption capacity of a sustainable Ultra-high performance fibre reinforced concrete (UHPFRC) in quasi-static mode and under high velocity projectile impact, Cem. Concr. Compos. 68 (2016) 109–122.
[10] R. Zhong, et al., Assessing the effectiveness of UHPFRC, FRHSC ECC High. Veloc. Proj. Impact Cem. Concr. Compos. 120 (2021) 104013.
[11] S. Kravanja, R. Sovják, Ultra-high-performance fibre-reinforced concrete under high-velocity projectile impact. Part I. Experiments, Acta Polytech. 58 (4) (2018) 232–239.
[12] M. Beppu, et al., Failure characteristics of UHPFRC panels subjected to projectile impact, Compos. Part B Eng. 182 (2020) 107505.
[13] Yoo, D.-Y., N. Banthia, and Y.-S. Yoon. Ultra high-performance fibre reinforced concrete under impact loading. in 7th RILEM conference on high-performance fiber reinforced cement composites (HPFRCC-7) at Stuttgart, June. 2015.
[14] D.-Y. Yoo, N. Banthia, Mechanical and structural behaviors of ultra-high-performance fiber-reinforced concrete subjected to impact and blast, Constr. Build. Mater. 149 (2017) 416–431.
[15] H. Wu, et al., Projectile penetration of ultra-high performance cement based composites at 510–1320 m/s, Constr. Build. Mater. 74 (2015) 188–200.
[16] P. Máca, R. Sovják, P. Konvalinka, Mix design of UHPFRC and its response to projectile impact, Int. J. Impact Eng. 63 (2014) 158–163.
[17] J. Liu, C. Wu, X. Chen, Numerical study of ultra-high performance concrete under non-deformable projectile penetration, Constr. Build. Mater. 135 (2017) 447–458.
[18] R. Sovják, et al., Experimental investigation of ultra-high performance fiber reinforced concrete slabs subjected to deformable projectile impact, Procedia Eng. 65 (2013) 120–125.
[19] E.F. O'Neil, B.D. Neeley, J.D. Cargile, Tensile properties of very-high-strength concrete for penetration-resistant structures, Shock Vib. 6 (5-6) (1999) 237–245.
[20] W. Anderson, A. Watson, P. Armstrong, Fiber reinforced concretes for the protection of structures against high velocity impact, Struct. Impact Crashworthiness 2 (1984) 687–695.
[21] A. Dancygier, D. Yankelevsky, High strength concrete response to hard projectile impact, Int. J. Impact Eng. 18 (6) (1996) 583–599.
[22] J. Liu, et al., Numerical investigation of reactive powder concrete reinforced with steel wire mesh against high-velocity projectile penetration, Constr. Build. Mater. 166 (2018) 855–872.
[23] J. Liu, et al., Experimental and numerical study of reactive powder concrete reinforced with steel wire mesh against projectile penetration, Int. J. Impact Eng. 109 (2017) 131–149.
[24] M. Maalej, S.T. Quek, J. Zhang, Behavior of hybrid-fiber engineered cementitious composites subjected to dynamic tensile loading and projectile impact, J. Mater. Civ. Eng. 17 (2) (2005) 143–152.
[25] V. Bindiganavile, N. Banthia, B. Aarup, Impact response of ultra-high-strength fiber-reinforced cement composite, Mater. J. 99 (6) (2002) 543–548.
[26] K. Habel, P. Gauvreau, Response of ultra-high performance fiber reinforced concrete (UHPFRC) to impact and static loading, Cem. Concr. Compos. 30 (10) (2008) 938–946.
[27] R. Yu, P. Spiesz, H.J.H. Brouwers, Static properties and impact resistance of a green Ultra-High Performance Hybrid Fibre Reinforced Concrete (UHPHFRC): experiments and modeling, Constr. Build. Mater. 68 (2014) 158–171.

[28] R. Sovják, et al., Resistance of slim UHPFRC targets to projectile impact using in-service bullets, Int. J. Impact Eng. 76 (2015) 166–177.
[29] G.-Y. Kim, et al., Response of UHPFRC and HDFRC under static and high-velocity projectile impact loads, Constr. Build. Mater. 188 (2018) 399–408.
[30] A. Ramesh, et al., Impact response of textile-reinforced 3D printed concrete panels, Eng. Struct. 315 (2024) 118489.
[31] G. Murali, A.S. Santhi, G.M. Ganesh, Effect of crimped and hooked end steel fibres on the impact resistance of concrete, J. Appl. Sci. Eng. 17 (3) (2014) 259–266.
[32] N. Banthia, C. Yan, K. Sakai, Impact resistance of fiber reinforced concrete at subnorma temperatures, Cem. Concr. Compos. 20 (5) (1998) 393–404.
[33] K.C.G. Ong, M. Basheerkhan, P. Paramasivam, Resistance of fibre concrete slabs to low velocity projectile impact, Cem. Concr. Compos. 21 (5-6) (1999) 391–401.
[34] J. Liu, et al., Ultra-high performance concrete targets against high velocity projectile impact–a-state-of-the-art review, Int. J. Impact Eng. 160 (2022) 104080.
[35] J. Liu, et al., A comprehensive review of ultra-high performance concrete (UHPC) behaviour under blast loads, Cem. Concr. Compos. (2024) 105449.
[36] M. Esaker, G.E. Thermou, L. Neves, Impact resistance of concrete and fibre-reinforced concrete: a review, Int. J. Impact Eng. (2023) 104722.
[37] B. Standard, Testing hardened concrete, Compress. Strength Test. Specim. BS EN (2009) 12390–12393.
[38] Y. Ou, D. Zhu, Tensile behavior of glass fiber reinforced composite at different strain rates and temperatures, Constr. Build. Mater. 96 (2015) 648–656.
[39] G.P.A.G. van Zijl, et al., Comparative testing of crack formation in strain-hardening cement-based composites (SHCC), Mater. Struct. 49 (2016) 1175–1189.
[40] A.J. Hamad, R.J.A. Sldozian, Flexural and flexural toughness of fiber reinforced concrete-American standard specifications review, GRD J. Glob. Res. Dev. J. Eng. 4 (3) (2019) 5–13.
[41] Q.M. Li, D.J. Tong, Perforation thickness and ballistic limit of concrete target subjected to rigid projectile impact, J. Eng. Mech. 129 (9) (2003) 1083–1091.
[42] H. Kim, et al., Static mechanical properties and impact resistance of amorphous metallic fiber-reinforced concrete, Compos. Struct. 134 (2015) 831–844.
[43] S. Hu, H. Tang, S. Han, Energy absorption characteristics of PVC coarse aggregate concrete under impact load, Int. J. Concr. Struct. Mater. 15 (1) (2021) 26.
[44] M.J. Forrestal, et al., An empirical equation for penetration depth of ogive-nose projectiles into concrete targets, Int. J. Impact Eng. 15 (4) (1994) 395–405.
[45] Michael, D., D. Norval, and P.C. Joseph, Structures to Resist the Effects of Accidental Explosions, Vol. 4, Reinforced Concrete Design. 1987, ARLCD-SP-84001.
[46] Samuely, F.J. and C.W. Hamann, *Civil protection*. 1939: Architectural Press.
[47] Gwaltney, R.C., Missile Generation and Protection in Light-water-cooled Power Reactor Plants. 1968, Oak Ridge National Lab., Tenn.
[48] P. Whiffen, UK Road. Res. Lab. Note No. MOS/311 (1943) **910**.
[49] Chelapati, C.V. and I.B. Wall, Probabilistic assessment of aircraft hazard for nuclear power plants. II 1970, Holmes and Narver, Inc., Los Angeles.
[50] Coleman, J.S., Summary Technical Report of Division 6, NDRC. Volume 15. Underwater Sound Equipment 2. Echo-Ranging Systems. 1946, OFFICE OF SCIENTIFIC RESEARCH AND DEVELOPMENT WASHINGTON DC NATIONAL DEFENSE ….
[51] R.P. Kennedy, A review of procedures for the analysis and design of concrete structures to resist missile impact effects, Nucl. Eng. Des. 37 (2) (1976) 183–203.
[52] A.K. Kar, Local effects of tornado-generated missiles, J. Struct. Div. 104 (5) (1978) 809–816.
[53] G. Hughes, Hard missile impact on reinforced concrete, Nucl. Eng. Des. 77 (1) (1984) 23–35.
[54] A. Haldar, H.A. Hamieh, Local effect of solid missiles on concrete structures, J. Struct. Eng. 110 (5) (1984) 948–960.
[55] H. Adeli, A.M. Amin, Local effects of impactors on concrete structures, Nucl. Eng. Des. 88 (3) (1985) 301–317.
[56] Bangash, M.Y.H., Concrete and concrete structures: Numerical modelling and applications. 1989.
[57] Q.M. Li, et al., Local impact effects of hard missiles on concrete targets, Int. J. Impact Eng. 32 (1-4) (2005) 224–284.
[58] Bangash, M.Y.H., Impact and explosion: structural analysis and design. 1993: Blackwell.
[59] G.E. Thermou, I. Hajirasouliha, Design-oriented models for concrete columns confined by steel-reinforced grout jackets, Constr. Build. Mater. 178 (2018) 313–326.
[60] J.H. Gonzalez-Libreros, et al., State of research on shear strengthening of RC beams with FRCM composites, Constr. Build. Mater. 149 (2017) 444–458.